Distributed Coverage Control of Mobile Sensor Networks Subject to Measurement Error

Jalal Habibi, *Senior Member, IEEE*, Hamid Mahboubi, *Senior Member, IEEE*, and Amir G. Aghdam, *Senior Member, IEEE*

Abstract—**Deployment algorithms proposed to improve coverage in sensor networks often rely on the Voronoi diagram, which is obtained by using the position information of the sensors. It is usually assumed that all measurements are sufficiently accurate, while in a practical setting, even a small measurement error may lead to significant degradation in the coverage performance. This paper investigates the effect of measurement error on the performance of coverage control in mobile sensor networks. It also presents a distributed deployment strategy, namely the Robust Max-Area strategy, which uses information on error bounds in order to move the sensors to appropriate locations. To this end, two polygons are obtained for each sensor, and it is shown that the exact Voronoi polygon (associated with accurate measurements) lies between them. A local spatial probability function is then derived for each sensor, which translates the available information about the error bound into the likelihood of the points being inside the exact Voronoi polygon. Subsequently, the deployment strategy positions each sensor such that the total covered area increases. The sensors' movements are shown to be convergent under the proposed strategy.**

Index Terms—**Coverage control, measurement error, mobile agents, Wireless sensor networks.**

I. Introduction

Wireless sensor networks have attracted much attention in the literature recently, due to their broad range of applications in different areas, such as weather monitoring, traffic management, and surveillance [1]–[3]. In particular, mobile sensor networks (MSNs) are very useful when the network configuration needs to be continuously adapted to the most current conditions of the environment. Typical objectives of an MSN include coverage maximization and target monitoring [4], [5]. In the coverage maximization problem, it is desired to locate the sensors in the field in such a way that the coverage holes in the network are minimized. In the target monitoring problem, on the other hand, the objective is to track a randomly moving target by establishing a route from the target to a destination point at all times.

One of the important issues in the design of an efficient MSN is to properly coordinate the movement of the sensors with limited communication between them. An effective cooperative control scheme plays an important role in the overall performance of the network. Any control strategy relies on the position information of other sensors. For example, in Voronoi-based coverage strategies, each sensor needs to know the position of its neighbors [6]. Different sensor deployment strategies are proposed in [7], and a sensitivity analysis for Voronoi-based algorithms is reported in [8]. The impact of communication noise on network coverage is investigated in [9], where it is shown that the optimal network configuration can be achieved by balancing the tradeoff between sensing and communication. The effect of imperfect communication links on coverage performance is discussed in [10]. A distributed coordination scheme is provided in [11] to address the problem of outdated location information in the deployment of mobile sensors. The problem of quantized information exchange among a group of robots is studied in [12], where a rate-constrained communication network is utilized by mobile agents. A motion coordination scheme is subsequently proposed for the rendezvous and deployment missions.

Probabilistic sensing models are also introduced in the literature, where the probability of an event to be sensed by a sensor is a value between 0 and 1. This type of uncertainty in sensing and relevant coverage problems are discussed in [13]–[16]. The problem of coverage optimization subject to uncertainty in the initial position of sensors is reported in [17]. A soft computing approach to manage the uncertainties in a sensor network is also reported in [18]. A distributed partitioning scheme is presented in [19] to determine the territory ownership for robots exploring a nonconvex region using unreliable pairwise communication.

While the above-mentioned articles address the problem of uncertainty or imperfect communication in sensor networks to some extent, they do not provide an efficient deployment strategy in the presence of measurement error. This paper is concerned with coverage optimization in a network of mobile sensors subject to inaccurate position information [20]. Given the maximum magnitude of error, a technique is provided to find two polygons for each sensor such that the exact Voronoi polygon is guaranteed to lie between them. A spatial probability function is defined accordingly for the margin between the two polygons, which is used to design a proper sensor deployment strategy.

Manuscript received August 31, 2015; revised November 30, 2015 and December 6, 2015; accepted December 9, 2015. Date of publication January 25, 2016; date of current version October 25, 2016. This work has been supported by the Natural Sciences and Engineering Research Council of Canada under Grant RGPIN-262127-12. Recommended by Associate Editor C. M. Lagoa.

J. Habibi is with the Faculty of Engineering, McGill University, Montréal, QC H3A 0C3, Canada (e-mail: jalal.habibi@mcgill.ca).

H. Mahboubi is with the Department of Electrical and Computer Engineering, McGill University, Montréal, QC H3A 0G4, Canada (e-mail: hamid.mahboobi@mail.mcgill.ca).

A. G. Aghdam is with the Department of Electrical and Computer Engineering, Concordia University, Montréal, QC H3G 1M8, Canada (e-mail: aghdam@ece.concordia.ca).

Color versions of one or more of the figures in this paper are available online at http://ieeexplore.ieee.org.

Digital Object Identifier 10.1109/TAC.2016.2521370

0018-9286 © 2016 IEEE. Translations and content mining are permitted for academic research only. Personal use is also permitted, but republication/redistribution requires IEEE permission. See http://www.ieee.org/publications_standards/publications/rights/index.html for more information.

The objective of the deployment strategy developed in the present work is to maximize the area covered by sensors. In [6], it is desired to minimize an objective function representing the total cost for all points of the field to access the sensors' locations. Deployment protocols in the above work are generalized in [11] to the case when the exchanged information is outdated. The main idea behind the motion coordination strategy in the above papers is to reduce the objective function by moving every sensor towards the centroid of either its Voronoi polygon or its bounding regions. The strategy relies on some differentiability properties that do not hold in the coverage maximization problem, and, hence, cannot be used for this objective. To address this shortcoming, gradient-based schemes are proposed in [21] and [22] for the area maximization problem. The present paper extends the scope of the above articles to the case of erroneous measurements. To the best of the authors' knowledge, this is the first work to investigate measurement error in the problem of area maximization in sensor networks.

The rest of this paper is structured as follows. Section II presents some theoretical background on sensor network coverage, as well as a model for measurement error. Some geometric concepts are used in Section III to analyze the effect of erroneous measurements on Voronoi polygons. Section IV uses the available information about the uncertainty to quantify the importance of coverage in different points around the Voronoi polygon. An efficient coverage control algorithm is then presented in Section V to optimally place the sensors in their polygons. Finally, the contributions of the paper are summarized in Section VI.

II. Preliminaries and Problem Statement

A. Voronoi-Based Coverage Control Strategies

Assume n mobile sensing agents $S_1, \ldots, S_n$ randomly placed in a 2D sensing field $\mathbb{F}$. It is assumed that the field has no obstacles and that the sensors have disk-shaped sensing patterns with radius R_s. The Voronoi diagram of the sensor network consists of n polygons denoted by $\Pi_1, \ldots, \Pi_n$. Polygon Π_i corresponds to sensor S_i and is mathematically defined as $\Pi_i = \{q \in \mathbb{F} | d(q, x_i) \leq d(q, x_j), j \in \mathbf{n} := \{1, \ldots, n\},\ j \neq i\}$, where x_i denoted the position of sensor S_i, and $d(q, x_i)$ is the Euclidean distance between x_i and an arbitrary point q. The field is said to be partitioned by the Voronoi cells if the cells do not intersect with each other and span the entire field. Two sensors are called neighbors if their Voronoi polygons share an edge. The set of indices of the neighboring sensors of sensor S_i is denoted by N_i, for any $i \in \mathbf{n}$.

The principles of a general class of distributed Voronoi-based coverage control protocols will now be reviewed. This class consists of algorithms that use distributed Voronoi partitioning and increase each sensor's covered area using local information. At any point in time, every sensor collects the position information of neighboring sensors and constructs its Voronoi polygon accordingly. Once all Voronoi cells are constructed, each sensor determines a candidate point inside its cell, according to a given strategy. For instance, in the Minimax strategy [7], the candidate point is the center of the smallest enclosing disk of the Voronoi polygon. The sensor will move to the candidate point only if its local coverage with respect to the current polygon increases from the new location; otherwise, it remains in its current position. Ideally, this procedure continues until the sensor network reaches a steady state but, in practice, a coverage improvement threshold is considered in order to stop sensors in finite time. It can be shown that under this type of local decision-making strategy, the total covered area will monotonically increase. As a performance measure of the coverage strategies, the ratio of the covered area to the overall area of the field is defined as the *coverage factor*. Various Voronoi-based algorithms are provided in the literature to determine the candidate point for each sensor, e.g., see [7], [21], and [23].

B. Modeling of the Measurement Error

Assume that each sensor has the exact information of its position and that the positions of neighboring sensors are measured either using a localization technique or by direct communication with them. Assume also that an upper bound on the position measurement error exists for each sensor. For any $j \in N_i$, denote by x_{ji} the position of sensor S_j, measured by sensor S_i, and let the corresponding measurement error be represented by e_{ji}. This means that, from the viewpoint of sensor S_i, sensor S_j lies within a disk D_j of radius e_{ji}, centered at x_{ji}. The size of the position error depends on the measurement method and is typically small, although its impact on the performance of the coverage algorithms may not be negligible. It is to be noted that for simulation purposes, a bounded random value (as the measurement error of sensor S_i) is added to the exact position of its neighboring sensor S_j. The resultant value is used as the erroneous measurement of sensor S_i. However, the error disk, noted earlier, around the real position of the neighboring sensor is not known to the measuring sensor (because knowing this disk implies that its center is known, which means that the exact measurement is also known). In the model used for the design of the deployment strategy, on the other hand, the problem is considered from the viewpoint of sensor S_i with information that is available to it. The sensor measures x_{ji} with a known error bound e_{ji}. Then, it assumes that the real position of sensor S_j lies in a disk of radius e_{ji} centered at the measured point x_{ji}, and based on this assumption, it constructs the bounding polygons. Both models imply that the distance between the measured position and real position of S_j is less than e_{ji}, and hence, the models are consistent. Note also that any sensor that measures the position of S_j constructs a disk around its measured point and is not aware of the measured values of other sensors. Thus, as far as the design procedure is concerned, it is more sensible to use the later model for error.

Given a probability density function for the position measurement error of each sensor, the location of the neighboring sensors can be characterized probabilistically. Without loss of generality, a uniform probability density function is considered in this paper for the position measurement error of every sensor. This implies that all points inside the above-mentioned disk have the same probability of being the real position of sensor S_j. This is demonstrated for an example of five sensors in

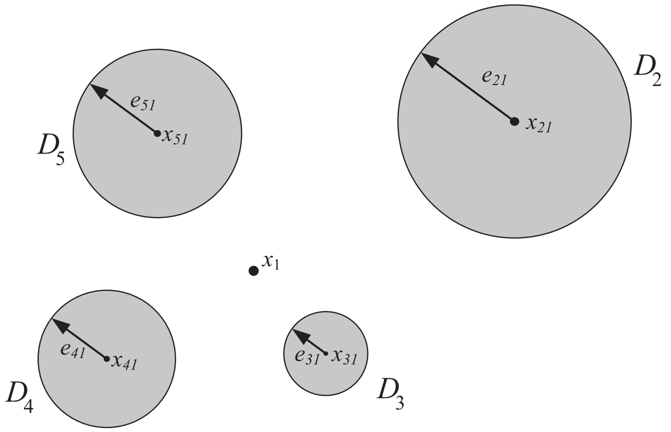

Fig. 1. Geometry of measurement error from the viewpoint of sensor S_1.

Fig. 1, where x_1 denotes the position of the measuring sensor S_1, and D_i, $i = 2, \ldots, 5$, represents the disk in which the ith sensor lies, from the measuring sensor's viewpoint.

C. Effect of Uncertainty on the Coverage Performance

The performance of the Voronoi-based coverage control algorithms in mobile sensor networks highly depends on the accuracy of the Voronoi partitioning. The Voronoi polygons obtained by erroneous partitioning may not be mutually exclusive or collectively exhaustive. This can negatively affect the convergence of the sensor deployment algorithms and the energy consumption of the sensors. The following example illustrates the performance deterioration of coverage control strategies in the presence of measurement error.

Example 1: Consider the coverage maximization problem for a network of 30 mobile sensors with a sensing range of 6 m in a 50 m × 50 m field, using the Minimax algorithm introduced in [7]. Initially, the sensors are assumed to be distributed randomly and are then driven by the Minimax strategy. To make the simulation statistically more realistic, 100 different initial configurations are randomly generated for the sensors. The coverage performance is then evaluated for the case of exact position information of the neighboring sensors as well as the case of erroneous measurements (for 10% and 15% measurement errors).

As a measure of convergence speed, the required number of rounds to reach steady state is also obtained. Simulations exhibit that, with exact information, the average number of rounds the Minimax deployment algorithm is executed to reach steady state is equal to nine, while with 10% and 15% error in position information, this number increases to 18 and 39 rounds, respectively. Fig. 2 provides the average number of moving sensors in each round versus time (the time unit considered here is the duration of each round in the Minimax algorithm) with perfect and erroneous measurements. As can be observed in this figure, with exact measurements, it takes 18 rounds in the worst case to converge to the final point. On the other hand, with 10% and 15% measurement error, the number of rounds in the worst case are 33 and 89, respectively, which translate to higher energy consumption. This example demonstrates that the measurement error can lead to higher energy consumption and slower convergence in a mobile sensor network. ■

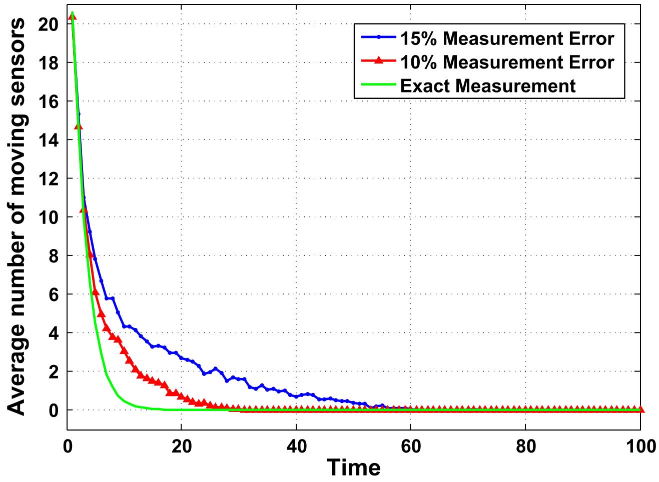

Fig. 2. Average number of moving sensors using Minimax approach with and without measurement error.

To achieve a better performance in the case of inaccurate measurements, an algorithm is presented in the sequel which uses a geometric approach to characterize the margins of the Voronoi cell corresponding to each sensor by an inner-bounding polygon and an outer-bounding polygon.

III. Geometric Characterization of Uncertainty in the Voronoi Partitioning

Given an upper bound on the magnitude of the measurement error, each sensor can construct a region in which the true Voronoi polygon (i.e., the Voronoi polygon in the ideal case of zero measurement error) lies. This region will hereafter be referred to as the *Voronoi margin*, and its size is directly related to the magnitude of the error bound. It is desired now to obtain inner and outer boundaries in the form of polygons for each Voronoi margin. It is also desired to characterize the relative importance of the points inside a Voronoi margin, which will later be used to develop an efficient coverage control strategy.

Corresponding to any sensor S_i, two pairs of rays (half-lines) are obtained for each neighboring sensor. It is shown that any facet of the true Voronoi polygon lies between the two pairs of rays associated with a neighboring node. These rays are subsequently used to obtain two polygons for each sensor such that the true Voronoi polygon lies between them. The objective is to find the above-mentioned pairs of rays for each neighboring node. A ray is mathematically described by a starting point q_0 and an angle θ_0 (where $-\pi < \theta_0 \leq \pi$) and is defined in $\mathbb{R}^2$ as follows:

$$R(q_0, \theta_0) = \left\{ q \in \mathbb{R}^2 | q = q_0 + \gamma \begin{bmatrix} \cos(\theta_0) \\ \sin(\theta_0) \end{bmatrix}, \ \gamma \geq 0 \right\} \quad (1)$$

Definition 1: Two rays $R_1(q_0, \theta_1)$ and $R_2(q_0, \theta_2)$, $\theta_1 \neq \theta_2$, which have the same starting point q_0 and distinct angles are called *joined rays* and denoted by $\{R_1, R_2\}$. A pair of joined

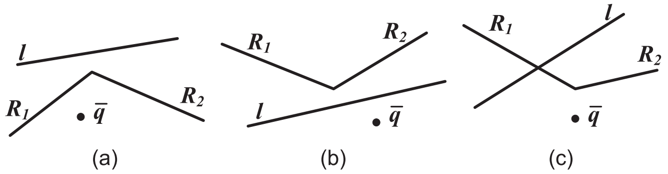

Fig. 3. Relative position of a line and two rays in a plane w.r.t. a point. (a) $\{R_1, R_2\}$ is an inner bound of the line l w.r.t. the point $\bar{q}$; (b) $\{R_1, R_2\}$ is an outer bound of the line l w.r.t. the point $\bar{q}$; and (c) $\{R_1, R_2\}$ is neither an inner bound nor an outer bound of the line l w.r.t. the point $\bar{q}$.

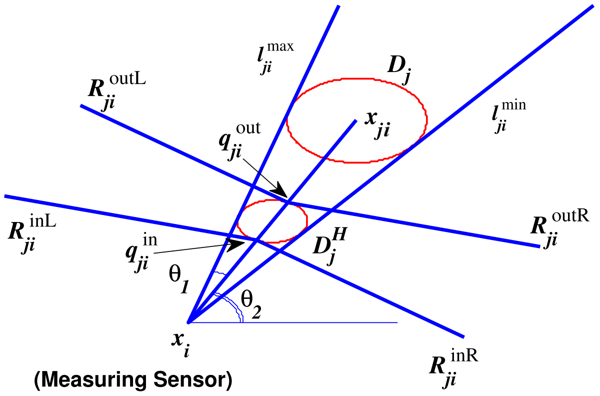

Fig. 4. Geometry of inner bounding and outer bounding rays of a facet of the Voronoi polygon.

rays partition $\mathbb{R}^2$ into two subsets. Given an arbitrary point $\bar{q}$, let the subset generated by the rays R_1 and R_2 and containing $\bar{q}$ be denoted by $F(R_1, R_2, \bar{q})$. The angle between two joined rays which contain the point $\bar{q}$ is called the *interior angle* w.r.t. $\bar{q}$.

Remark 1: If the interior angle w.r.t. the point $\bar{q}$ is less than π, then a point q is in $F(R_1, R_2, \bar{q})$ when q and $\bar{q}$ are on the same side of both lines corresponding to rays R_1 and R_2. Similarly, if the interior angle w.r.t. the point $\bar{q}$ is greater than π, then a point q is in $F(R_1, R_2, \bar{q})$ when q and $\bar{q}$ are on the same side of either of the lines corresponding to rays R_1 and R_2.

Definition 2: Consider a point $\bar{q}$, a line l, and two joined rays R_1 and R_2 in $\mathbb{R}^2$. The pair $\{R_1, R_2\}$ is said to be an *inner bound* of the line l w.r.t. $\bar{q}$ if any point in $\mathbb{R}^2$ that is on the same side of $\{R_1, R_2\}$ as $\bar{q}$ is also on the same side of l that $\bar{q}$ is located. In other words, for a given point q, if $q \in F(R_1, R_2, \bar{q})$, then q and $\bar{q}$ are on the same side of the line l. Similarly, $\{R_1, R_2\}$ is said to be an *outer bound* of the line l w.r.t. $\bar{q}$ if any point in $\mathbb{R}^2$ that is on the same side of l as $\bar{q}$ is also on the same side of $\{R_1, R_2\}$ as $\bar{q}$. Obviously, a pair of joined rays might be neither an inner-bound nor an outer-bound of a line w.r.t. a given point. Fig. 3 provides illustrative examples of the above-mentioned cases.

To find an inner bound and an outer bound of a facet of Voronoi cell, one can consider the geometry shown in Fig. 4. The real position of sensor S_j, denoted by $\tilde{x}_j$, is somewhere in the disk $D_j = \{q \in \mathbb{R}^2 | \|q - x_{ji}\| \leq e_{ji}\}$. Let D_j^H be a disk obtained by downscaling D_j by a factor of 1/2 as

$$D_j^H = \left\{ q \in \mathbb{R}^2 \,\middle|\, \left\| q - \frac{1}{2}(x_i + x_{ji}) \right\| \leq \frac{1}{2} e_{ji} \right\}. \tag{2}$$

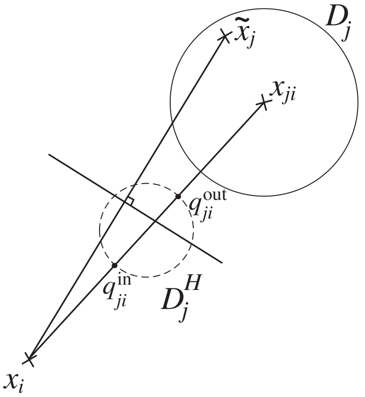

Fig. 5. Geometry of a general perpendicular bisector discussed in Lemma 1.

Note that the midpoint of the segment connecting x_i to $\tilde{x}_j$ (which is the foot of the corresponding perpendicular bisector) is located in the disk D_j^H. Denote the unit vector pointing from x_i to x_{ji} by r_{ji}, i.e.,

$$r_{ji} = \frac{x_{ji} - x_i}{\|x_{ji} - x_i\|}. \tag{3}$$

Note that there is an innermost point as well as an outermost point on the boundary of the disk D_j^H w.r.t. S_i. These points are denoted by q_{ji}^{in} and q_{ji}^{out}, respectively, and are mathematically expressed as

$$q_{ji}^{\text{in}} = \frac{1}{2}(x_i + x_{ji}) - \frac{1}{2} e_{ji} r_{ji} \tag{4}$$

$$q_{ji}^{\text{out}} = \frac{1}{2}(x_i + x_{ji}) + \frac{1}{2} e_{ji} r_{ji}. \tag{5}$$

The next lemma is used later to prove some important geometric properties of the bounding rays.

Lemma 1: Assume that the real position of sensor S_j (denoted by $\tilde{x}_j$) is somewhere in the disk D_j. Then, the perpendicular bisector of the segment $x_i\tilde{x}_j$ intersects the line passing through x_i and x_{ji} at some point between q_{ji}^{in} and q_{ji}^{out}.

Proof: Fig. 5 depicts the geometry considered in this lemma. Let the distance between x_i and x_{ji} be denoted by d_{ji}. Define a Cartesian coordinate system q_2q_1 whose origin is, in fact, at $(1/2)(x_i + x_{ji})$ (which is also the center of the disk D_j^H) with the q_2 axis directed towards x_{ji}, and q_1 perpendicular to it. Therefore, $x_i = [0, -(1/2)d_{ji}]$ and $x_{ji} = [0, (1/2)d_{ji}]$. An arbitrary point $q_\perp$ in D_j^H represents the foot of a perpendicular to the segment $x_i\tilde{x}_j$, for $\tilde{x}_j$ somewhere in the disk D_j. Such a point can be parametrically characterized as $q_\perp = [r\cos(\alpha), r\sin(\alpha)]^T$, where $0 \leq r \leq (1/2)e_{ji}$ and $0 \leq \alpha < 2\pi$. Therefore, the perpendicular bisector of the segment $x_i\tilde{x}_j$ passes through $q_\perp$ is characterized as

$$q_2 - r\sin(\alpha) = -\frac{r\cos(\alpha)}{r\cos(\alpha) + \frac{1}{2}d_{ji}} \left(q_1 - r\cos(\alpha)\right). \tag{6}$$

Now, set q_1 in the above equation to zero in order to find the intersection of this line and the q_2 axis (i.e., q_2-intercept value) as follows:

$$q_{2\perp} = \frac{r^2 + \frac{1}{2}d_{ji}r\sin(\alpha)}{r\sin(\alpha) + \frac{1}{2}d_{ji}}. \tag{7}$$

In fact, a general perpendicular to the segment $x_i q_\perp$ can be expressed as

$$q_2 - m q_1 - q_{2\perp} = 0. \tag{8}$$

It is desired now to show that the point $[0, q_{2\perp}]^T$ is located somewhere between q_{ji}^{in} and q_{ji}^{out}. To this end, it is noted that $q_{2\perp}$ is a function of two independent variables r and $\sin(\alpha)$. Denote $\sin(\alpha)$ by y; the minimum and maximum values of $q_{2\perp}(r, y)$ over the region $D_{ry} = \{0 \leq r \leq (1/2)d_{ji}, -1 \leq y \leq 1\}$ are needed to proceed further. First, notice that the partial derivative of $q_{2\perp}$ w.r.t. y is given by

$$\frac{\partial}{\partial y} q_{2\perp} = \frac{\partial}{\partial y}\left[\frac{r^2 + 1\frac{2}{d_{ji}} r y}{r y + \frac{1}{2} d_{ji}}\right] = \frac{r\left(1\frac{2}{d_{ji}}\right)^2 - r^3}{\left(r y + \frac{1}{2} d_{ji}\right)^2} \tag{9}$$

which is obviously non-negative as $(1/2)d_{ji} \geq (1/2)e_{ji} \geq r$. This means that $q_{2\perp}$ takes its maximum and minimum values on the boundaries $y = 1$ and $y = -1$. It is straightforward to verify that $y = 1$ and $y = -1$ are associated with the respective values $\max(r)$ and $-\max(r)$ for $q_{2\perp}$. This means that $-(1/2)e_{ji} \leq q_{2\perp} \leq (1/2)e_{ji}$. ■

Upper and lower bounds on m (the slope of the perpendicular bisector (8)) can also be obtained by considering the maximum and minimum slope of a line passing through x_i and an arbitrary point inside D_j (in Fig. 4, the lines with minimum and maximum slopes are depicted by $l_{ji}^{\min}$ and $l_{ji}^{\max}$). Let the angles θ_1 and θ_2 in Fig. 4 be defined as follows:

$$\theta_1 = \sin^{-1}\left(\frac{e_{ji}}{d_{ji}}\right) \tag{10}$$

$$\theta_2 = \angle(x_{ji} - x_i) = \tan^{-1}\left(\frac{(x_{ji} - x_i)_2}{(x_{ji} - x_i)_1}\right) \tag{11}$$

where $(.)_1$ and $(.)_2$ denote the components of a vector along the q_1 and q_2 axes, respectively, and the angle $\tan^{-1}(.)$ lies in the interval $[-\pi, \pi]$. The angle of a line passing through x_i and $\tilde{x}_j$ is between $\theta_2 - \theta_1$ and $\theta_2 + \theta_1$. Hence, the slope of the corresponding perpendicular line is bounded by

$$m_{\perp 1} = -\frac{1}{\tan(\theta_2 + \theta_1)} \tag{12}$$

$$m_{\perp 2} = -\frac{1}{\tan(\theta_2 - \theta_1)}. \tag{13}$$

The following theorem states that the perpendicular bisector (a segment of which is the facet of the Voronoi polygon Π_i) lies between the rays drawn from innermost and outermost points with minimum and maximum slopes.

Theorem 1: The true Voronoi facet between each (S_i, S_j) pair is inner-bounded by a pair of joined rays R_{ji}^{inL} and R_{ji}^{inR} defined as follows:

$$R_{ji}^{\text{inL}} = R\left(q_{ji}^{\text{in}}, \theta_{ji}^{\text{inL}}\right) \tag{14}$$

$$R_{ji}^{\text{inR}} = R\left(q_{ji}^{\text{in}}, \theta_{ji}^{\text{inR}}\right) \tag{15}$$

where

$$\theta_{ji}^{\text{inR}} = \theta_2 - \theta_1 - \frac{\pi}{2} \tag{16}$$

$$\theta_{ji}^{\text{inL}} = \theta_2 + \theta_1 + \frac{\pi}{2} \tag{17}$$

(note that the superscripts R and L represent, respectively, the right and left rays from the viewpoint of S_i). Also, the aforementioned facet is outer-bounded by a pair of rays R_{ji}^{outL} and R_{ji}^{outR} defined as follows:

$$R_{ji}^{\text{outL}} = R\left(q_{ji}^{\text{out}}, \theta_{ji}^{\text{outL}}\right) \tag{18}$$

$$R_{ji}^{\text{outR}} = R\left(q_{ji}^{\text{out}}, \theta_{ji}^{\text{outR}}\right) \tag{19}$$

where

$$\theta_{ji}^{\text{outR}} = \theta_2 + \theta_1 - \frac{\pi}{2} \tag{20}$$

$$\theta_{ji}^{\text{outL}} = \theta_2 - \theta_1 + \frac{\pi}{2}. \tag{21}$$

Proof: Let the q_2 axis be the same as the one introduced in the previous lemma. Consider a lower bound and an upper bound on the slope of the perpendicular bisector denoted by $m_{\min} = \min\{m_{\perp 1}, m_{\perp 2}\}$ and $m_{\max} = \max\{m_{\perp 1}, m_{\perp 2}\}$, respectively. Then, the inner-bounding rays are parts of the following lines:

$$q_2 - m_{\min} q_1 - \left(q_{ji}^{\text{in}}\right)_2 = 0 \tag{22}$$

$$q_2 - m_{\max} q_1 - \left(q_{ji}^{\text{in}}\right)_2 = 0. \tag{23}$$

Similarly, the outer-bounding rays are parts of the following lines:

$$q_2 - m_{\min} q_1 - \left(q_{ji}^{\text{out}}\right)_2 = 0 \tag{24}$$

$$q_2 - m_{\max} q_1 - \left(q_{ji}^{\text{out}}\right)_2 = 0. \tag{25}$$

Note that the interior angle of the subset $F(R_{ji}^{\text{inR}}, R_{ji}^{\text{inL}}, x_i)$ is equal to $\pi - 2\theta_1$. Since the error e_{ji} is assumed to be less than d_{ji}, the angle θ_1 is less than $\pi/2$ and, hence, $\pi - 2\theta_1$ is between 0 and π. Therefore, a point belongs to $F(R_{ji}^{\text{inR}}, R_{ji}^{\text{inL}}, x_i)$ if it is on the same side as S_i with respect to both lines (22) and (23). Similarly, the interior angle of $F(R_{ji}^{\text{outR}}, R_{ji}^{\text{outL}}, x_i)$ is $\pi + 2\theta_1$, which is greater than or equal to π. Thus, a point belongs to $F(R_{ji}^{\text{outR}}, R_{ji}^{\text{outL}}, x_i)$ if it is on the same side as S_i with respect to either of the lines (24) and (25).

To prove the first part of the theorem, it is noted that for the point $x_i = [0, -(1/2)d_{ji}]$

$$(x_i)_2 - m_{\min}(x_i)_1 - \left(q_{ji}^{\text{out}}\right)_2 = -\frac{1}{2}d_{ji} - \frac{1}{2}e_{ji} \leq 0 \tag{26}$$

$$(x_i)_2 - m_{\max}(x_i)_1 - \left(q_{ji}^{\text{out}}\right)_2 = -\frac{1}{2}d_{ji} - \frac{1}{2}e_{ji} \leq 0. \tag{27}$$

Consider an arbitrary point $\bar{q} = [\bar{q_1}, \bar{q_2}]^T$ on the same side of the inner-bounding rays that S_i is located, i.e.,

$$\bar{q_2} - m_{\min}\bar{q_1} - \left(q_{ji}^{\text{in}}\right)_2 \leq 0 \tag{28}$$

$$\bar{q_2} - m_{\max}\bar{q_1} - \left(q_{ji}^{\text{in}}\right)_2 \leq 0. \tag{29}$$

It is desired to show that $\bar{q}$ is also on the same side of the perpendicular (8) that S_i lies, i.e.,

$$\bar{q}_2 - m\bar{q}_1 - q_{2\perp} \leq 0. \tag{30}$$

On the other hand, the inequality $\left(q_{ji}^{\mathrm{in}}\right)_2 \leq q_{2\perp}$ implies that

$$\bar{q}_2 - q_{2\perp} \leq \bar{q}_2 - \left(q_{ji}^{\mathrm{in}}\right)_2. \tag{31}$$

Since $m_{\min} \leq m \leq m_{\max}$, one can conclude that for any positive $\bar{q}_1$

$$-m\bar{q}_1 \leq -m_{\min}\bar{q}_1. \tag{32}$$

By adding (32) and (31) and using (28), the inequality (30) is deduced for $\bar{q}_1 \geq 0$. Similarly, for negative values of $\bar{q}_1$

$$-m\bar{q}_1 \leq -m_{\max}\bar{q}_1. \tag{33}$$

By adding (33) and (31) and using (29), the inequality (30) is resulted for any $\bar{q}_1 \leq 0$.

The result for outer-bounding rays is that if a point $\bar{q} = [\bar{q}_1, \bar{q}_2]^T$ lies on the same side of the perpendicular line (8) that S_i is located (as described by (30)), then at least one of the following two relations holds:

$$\bar{q}_2 - m_{\max}\bar{q}_1 - \left(q_{ji}^{\mathrm{out}}\right)_2 \leq 0 \tag{34}$$

$$\bar{q}_2 - m_{\min}\bar{q}_1 - \left(q_{ji}^{\mathrm{out}}\right)_2 \leq 0. \tag{35}$$

Similarly, it is straightforward to show that the inequality $q_{2\perp} \leq \left(q_{ji}^{\mathrm{out}}\right)_2$ yields

$$\bar{q}_2 - \left(q_{ji}^{\mathrm{out}}\right)_2 \leq \bar{q}_2 - q_{2\perp}. \tag{36}$$

For positive values of $\bar{q}_1$, it is obvious that

$$-m_{\max}\bar{q}_1 \leq -m\bar{q}_1. \tag{37}$$

By adding (36) and (37) and using (30), one arrives at (34). Similarly, for negative values of $\bar{q}_1$

$$-m_{\min}\bar{q}_1 \leq -m\bar{q}_1. \tag{38}$$

Adding (36) and (38) and using (30) leads to (35). ■

The following corollary on the convexity of the set generated by the inner-bounding rays is a direct result of the previous theorem.

Corollary 1: The set $F(R_{ji}^{\mathrm{inR}}, R_{ji}^{\mathrm{inL}}, x_i)$ is convex.

Proof: The above set is characterized by the points for which both (28) and (29) hold. These inequalities represent convex sets in $\mathbb{R}^2$, and, hence, their intersection is a convex region as well. ■

Remark 2: Due to the singularity of $\tan(\theta)$ at $\theta = \pi/2$, theoretically the slope of the perpendicular line (8) may lie in the interval $(-\infty, m_{\perp 2}] \cup [m_{\perp 1}, +\infty)$. This, however, does not affect the proof of Theorem 1 because if the q_2-axis and the line passing through x_i and x_{ji} coincide, then the slope of the perpendicular line is between $m_{\min} < 0$ and $m_{\max} > 0$.

The concepts of the inner bound and outer bound of a facet will now be used to find the inner- and outer-bounding polygons of the true Voronoi polygon. To this end, these polygons need to be characterized mathematically.

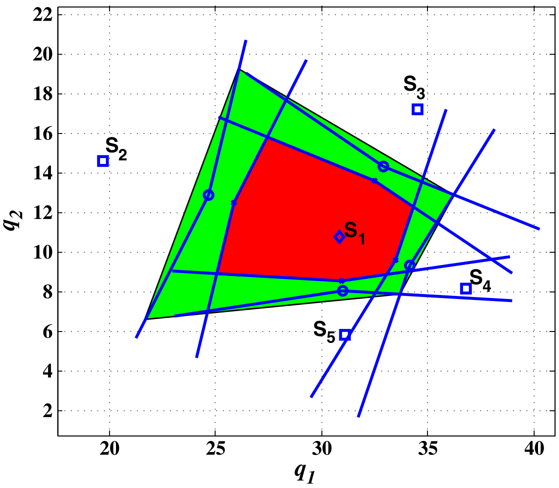

Fig. 6. A simple example of inner-bounding and outer-bounding polygons for a sensor with four neighbors.

Definition 3: Consider $\dim(N_i)$ pairs of outer-bounding rays $\{R_{ji}^{\mathrm{outR}}, R_{ji}^{\mathrm{outL}}\}$ for $j \in N_i$ and define the following subset of $\mathbb{R}^2$:

$$F_i^{\mathrm{out}} = \mathbb{F} \cap \left[\bigcap_{j \in N_i} F\left(R_{ji}^{\mathrm{outR}}, R_{ji}^{\mathrm{outL}}, x_i\right)\right] \tag{39}$$

(note that this set can be nonconvex, in general). Define also the smallest convex envelope of F_i^{out} as the *outer-bounding polygon* of the true Voronoi polygon containing S_i and denote it by Π_i^{outer}. Similarly, consider $\dim(N_i)$ pairs of inner-bounding rays $\{R_{ji}^{\mathrm{inR}}, R_{ji}^{\mathrm{inL}}\}$, $j \in N_i$. Every subset $F(R_{ji}^{\mathrm{inR}}, R_{ji}^{\mathrm{inL}}, x_i)$, $j \in N_i$, is convex and the *inner-bounding polygon* is defined as

$$\Pi_i^{\mathrm{inner}} = \mathbb{F} \cap \left[\bigcap_{j \in N_i} F\left(R_{ji}^{\mathrm{inR}}, R_{ji}^{\mathrm{inL}}, x_i\right)\right] \tag{40}$$

(the field $\mathbb{F}$ in expressions (39) and (40) specifies the area desired to be covered).

Definition 4: The set of all points between the inner-bounding and outer-bounding polygons of a sensor (i.e., $\Pi_i^{\mathrm{outer}} - \Pi_i^{\mathrm{inner}}$) is referred to as the *Voronoi margin*.

An example of the inner-bounding and outer-bounding polygons obtained by intersecting the inner and outer rays as described above is given in Fig. 6. The following theorem states that the true Voronoi polygon corresponding to any sensor lies between the inner-bounding and outer-bounding polygons of that sensor.

Theorem 2: Assume that every node in a sensor network constructs the inner-bounding and outer-bounding polygons defined above, using the neighboring sensors' position measurements and available information about the error bounds. Then, $\Pi_i^{\mathrm{inner}} \subseteq \Pi_i \subseteq \Pi_i^{\mathrm{outer}}$, where Π_i is the true Voronoi polygon corresponding to sensor S_i.

Proof: Denote the size of the neighboring set N_i by $\dim(N_i)$, and let the points inside the polygon Π_i be described by the inequality $Hq - K \leq 0$, where $H \in \mathbb{R}^{\dim(N_i)\times 2}$ and $K \in \mathbb{R}^{\dim(N_i)\times 1}$ (note that the facets of the polygon are given

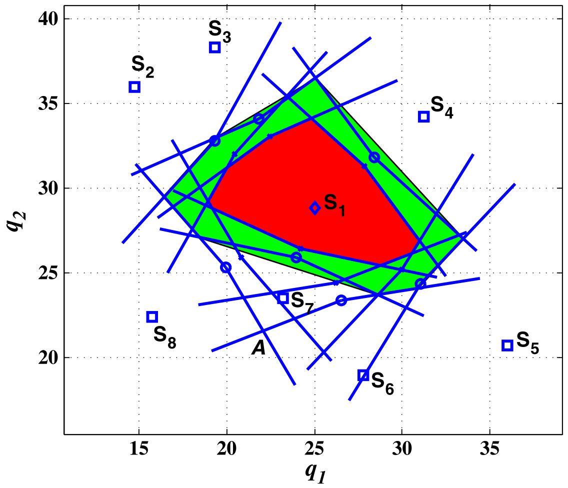

Fig. 7. Illustrative example for the case when the outer-bounding polygon is not the same as the convex hull created by the outer-bounding rays.

by $Hq - K = 0$). Let also q be a point in Π_i^{inner}. Relation (40) implies that $q \in F(R_{ji}^{\text{inR}}, R_{ji}^{\text{inL}}, x_i)$ for all $j \in N_i$. It follows from the previous theorem that $(H)_j q - (K)_j \le 0$, where $(.)_j$ represents the jth row of the corresponding matrix. This obviously means that $q \in \Pi_i$. Using a similar approach, assuming that $q \in \Pi_i$, it can also be shown that $q \in F_i^{\text{out}}$, and note that F_i^{out} is a subset of Π_i^{outer}. ■

Remark 3: Although in the simple configuration shown in Fig. 6 the outer-bounding polygon turns out to be the same as the convex hull created by the outer-bounding rays, this is not necessarily the case in general (even when these polygons are completely inside the field, and have no intersection with its boundaries). This is illustrated in Fig. 7 for a sensor S_1 with seven neighboring sensors S_2-S_8. It can be observed that the point A in this figure is the intersection point of the outer-bounding rays for S_6 and S_8, but it does not belong to the outer-bounding polygon. The inner-bounding polygon, however, is always the convex hull created by the inner-bounding rays.

Geometric algorithms are provided in Appendix A, which can be used to find the inner-bounding and outer-bounding polygons. These algorithms rely only on information available to each sensing agent and, hence, can be implemented in a distributed fashion. Using these algorithms, each sensor can find its inner- and outer-bounding polygons.

As far as coverage is concerned, the points in the inner-bounding polygon cannot be covered by any neighboring sensor if they are not covered by the sensor inside that polygon. From a probabilistic viewpoint, all points inside the inner-bounding polygon belong to the true Voronoi polygon as well, with probability 1. On the other hand, for the points inside the Voronoi margin, this probability varies between 0 and 1. More precisely, the points closer to the inner-bounding polygon are more likely to lie inside the true Voronoi polygon, as well. This implies that the points inside the inner-bounding polygon are the most important points to be covered by the sensor inside that polygon.

Remark 4: It is to be noted that each deployment strategy may require a specific partitioning algorithm. The effect of uncertainty on the Voronoi diagram is also investigated in [24], where uncertain information is used to find an approximate shape for the inner-bounding polygon only. Bounding regions for the case of inaccurate or outdated information are also presented in [11] and [25]. The deployment scheme in [11] aims at minimizing the total access cost as noted earlier in Section I. The results of the above work show that if every sensor moves towards the centroid of its Voronoi polygon, the cost function decreases. In the presence of outdated information, the dual-guaranteed Voronoi diagram introduced in [11] can be used to ensure that the cost function decreases. To this end, the inner-bounding and outer-bounding cells do not need to be convex. Our approach, on the other hand, aims at maximizing the covered area, and the underlying optimization strategy (i.e., the Max-Area technique) deals with convex polygons. In addition, to efficiently locate the sensing disk, it is important to characterize the points between the inner-bounding and outer-bounding polygons in terms of likelihood of being inside the true Voronoi polygon. This leads to the introduction of the local spatial probability functions, which will be described in the next section.

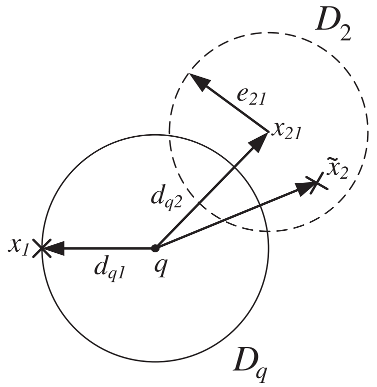

Fig. 8. Illustrative example for the probabilistic analysis concerning two sensors subject to position measurement error.

IV. Spatial Probability Function for the Voronoi Margin

It is desired now to systematically formulate the effect of measurement error in a sensor network by properly assigning a probability (as discussed in the previous section) to every point in the Voronoi margin. This probability provides a metric for the degree of importance of coverage for different points and is used as a priority function over the field.

To illustrate the idea with a simple example, consider a network of two mobile sensors S_1 and S_2. Let the real position of sensor S_2 be represented by $\tilde{x}_2$, and the maximum measurement error be denoted by e_{21}. For simplicity of notation, let the distances $d(q, x_1)$ and $d(q, x_2)$ be denoted by d_{q1} and d_{q2}, respectively. It is desired to find the probability

$$P_{21}(q) = \text{Prob}\left[d_{q1} \le d(q, \tilde{x}_2)\right] \quad (41)$$

for any point q (note that in the above expression $d(q, \tilde{x}_2)$ is a probabilistic quantity, while d_{q1} is deterministic).

Given the sensor configuration in Fig. 8, draw a circle of radius d_{q1} centered at q and denote it by D_q. The real position of

S_2 is somewhere inside the dashed circle of radius e_{21} centered at x_2 (i.e., the measured location of S_2). If these two circles do not intersect, then P_{21} is either zero (complete overlap) or one (no overlap at all). For the case when they intersect, P_{21} can be found using the area between two intersecting circles. This area is a known function of the radii of two circles and the distance of their centers as follows [26]:

$$\begin{aligned} A_{qx_2} =& d_{q1}^2 \cos^{-1}\left(\frac{d_{q2}^2 + d_{q1}^2 - e_{21}^2}{2d_{q2}d_{q1}}\right) \\ &+ e_{21}^2 \cos^{-1}\left(\frac{d_{q2}^2 + e_{21}^2 - d_{q1}^2}{2d_{q2}e_{21}}\right) \\ &- \frac{1}{2}\sqrt{\left[(e_{21}+d_{q1})^2 - d_{q2}^2\right]\left[d_{q2}^2 - (d_{q1}-e_{21})^2\right]}. \end{aligned} \tag{42}$$

Hence, P_{21} can be obtained as

$$P_{21}(q) = \begin{cases} 0, & d_{q1} > d_{q2} + e_{21} \\ \hat{P}_{21}(q), & d_{q2} - e_{21} \le d_{q1} \le d_{q2} + e_{21} \\ 1, & d_{q1} < d_{q2} - e_{21} \end{cases} \tag{43}$$

where

$$\hat{P}_{21}(q) = 1 - \frac{A_{qx_2}}{\pi e_{21}^2}. \tag{44}$$

The spatial probability function for the Voronoi margin, which is denoted by $\varphi_i(q)$, can now be derived by extending the relation obtained for $P_{21}(q)$ to any sensor configuration with an arbitrary number of sensors as follows:

$$\begin{aligned} \varphi_i(q) =& \text{Prob}\{q \in \Pi_i\} \\ =& \prod_{j \in N_i} \text{Prob}\left[d_{qi} \le d(q, \tilde{x}_j)\right] = \prod_{j \in N_i} P_{ji}(q). \end{aligned} \tag{45}$$

An example of the probability function around the true Voronoi polygon of a sensor as described above is depicted in Fig. 9 for the case when the magnitude of error is $e_{ji} = 0.1d_{ji}$. The three color contours correspond to three different level sets $\varphi_i(q) = 0,\ 0.5,\ 1$. More precisely, the small contour is the largest closed-path such that every point on it (and inside it) is guaranteed to belong to the true Voronoi polygon, and the large contour is the smallest closed path such that every point on it (and outside it) is guaranteed not to belong to the true Voronoi polygon with probability 1. Every point on the middle contour, on the other hand, belongs to the true Voronoi polygon with probability 0.5 for the given setup. As expected, the inner-bounding polygon (which is the small polygon in this figure) is enclosed by the contour corresponding to $\varphi_i(q) = 1$, and the outer-bounding polygon (which is the large polygon in this figure) encloses the contour corresponding to $\varphi_i(q) = 0$.

It is known that the contours corresponding to $\varphi_i(q) = 1$ and $\varphi_i(q) = 0$ can also be characterized as a set of hyperbolic curves [11]. For instance, considering the geometry shown in Fig. 8, the boundary between the two sensors with $\varphi_1(q) = 1$ can be characterized as the boundary of the region where $\text{Prob}[d_{q1} \le d(q, \tilde{x}_2)] = 1$ or, equivalently, $d_{q1} \le \min_{\tilde{x}_2 \in D_2} d(q, \tilde{x}_2) = d_{q2} - e_{21}$. Hence, the boundary is characterized by a hyperbola as $d_{q2} - d_{q1} = e_{21}$. Therefore, considering all neighboring sensors, the boundary corresponding to $\varphi_1(q) = 1$ can be expressed as the intersection of several hyperbolas. The concept of bounding polygons can help to find approximate regions efficiently in order to apply coverage strategies.

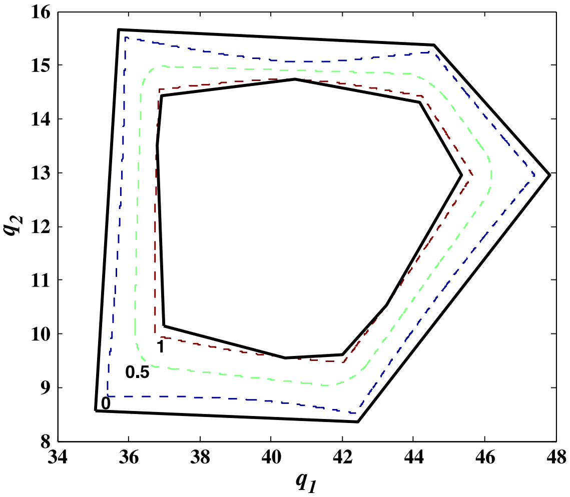

Fig. 9. Inner-bounding and outer-bounding polygons and three different level sets for a typical local spatial probability function $\varphi_i(q)$.

One can draw the contours described above for different values of φ_i between 0 and 1 in Fig. 9 (given the value of position measurement error e_{ji} for different $j \in N_i$). For simplicity of computation, however, one can use the inner- and outer-bounding polygons instead. As an approach for coverage improvement, the inner polygon of every sensor can be used to partition the field, in which case some points in the field will not be inside any of these polygons (assuming that there is at least one sensor with erroneous measurement). In this case, there is a better chance that the most important points (i.e., the points inside the inner polygons) are covered by using a proper sensor-deployment strategy. Alternatively, one can use the outer-bounding polygons to partition the field, in which case some points inside a polygon will be covered by some other polygons as well. These two approaches are further discussed in Section V.

The importance of the probabilistic characterization described above is that it transforms information about the measurement error bound into a function representing the relative importance of the points in terms of coverage. This leads to a prioritized sensing field with overlapping polygons, where the coverage priority of different points in each polygon is characterized by a local spatial probability function.

Remark 5: In the procedure described above for computing the local spatial probability function $\varphi_i(q)$, it is assumed that the distribution of the measurement error is uniform. In practice, however, it is often the case that the points closer to the measured positions are more probable to be the real location of the corresponding neighboring sensor. For example, in the simple configuration of Fig. 8, the real position of sensor S_2 is more likely to be closer to the center of the disk D_{S_2}. In general, the spatial probability function φ_i depends on the statistical characteristics of the error e_{ij}. Given a nonuniform distribution for measurement error, similar steps can be taken to find the corresponding local spatial probability function. For instance, for the case of a Gaussian measurement error, finding $P_{21}(q)$ in (41) would require double integration of the Gaussian density function over the disk D_q in Fig. 8.

V. Coverage Control

A. Robust Max-Area Deployment Strategy

Thus far, it is shown that using the upper bounds of the measurement error, a local spatial probability function can be defined around each sensor. As noted earlier, this function reflects the relative importance of different points in the field for coverage purposes. It was also shown that one can use a systematic approach to construct two polygons which the contours of the spatial probability function lie between them. It is desired in the sequel to use the results obtained so far to develop a distributed coverage control strategy for coordinating the movement of the sensors in order to maximize coverage. To this end, the function $\varphi_i(q)$, $i \in \mathbf{n}$, is employed as a weight function to prioritize the coverage of different points in the field accordingly. A sensor deployment strategy is subsequently used to find the optimal candidate point for each sensor (inside its outer-bounding polygon) to move to. In order to describe the algorithm, the following geometric optimization problem is introduced first.

Optimal Sensor Location (OSL) Problem: Consider a sensor S located at x_s inside a polygon Π, with a disk-shaped sensing pattern D of radius R_s, centered at x_s. Assume that a spatial probability function denoted by $\varphi(q)$ is available over Π, which is used as a weight function to formulate the relative importance of different points inside Π in terms of coverage. The *optimal sensor location* problem is concerned with finding a proper location x_s^* for the sensor to move to, such that the weighted coverage within the intersection of the sensing disk D and the polygon Π is maximized, i.e.,

$$x_s^* = \arg\max_{x_s\in\Pi} F(x_s) = \arg\max_{x_s\in\Pi} \int\limits_{\Pi\cap D} \varphi(q)dq. \tag{46}$$

■

Consider now the problem of coverage maximization in a sensor network subject to position measurement error. Let S be a sensor in the network whose inner-bounding and outer-bounding polygons are denoted by Π^{inner} and Π^{outer}, respectively. The optimal solution of the OSL problem can be obtained by using a gradient-based approach. One can assume $\Pi = \Pi^{\text{outer}}$, and use the iterative nonlinear optimization approach given in [22], i.e., the Max-Area technique, and solve the underlying nonlinear optimization problem by reformulating (46) as

$$x_s^* = \arg\min_{x_s\in\Pi} f(x_s) = \arg\min_{x_s\in\Pi} \left[-\int\limits_{\Pi\cap D} \varphi(q)dq\right] \tag{47}$$

where $f(x_s) := -F(x_s)$. Denoting the optimization variable in the kth iteration by x_k, the Max-Area approach updates this variable using the relation

$$x_{k+1} = x_k + \alpha_k p_k \tag{48}$$

where the vector p_k is a gradient-based search direction, and the scalar α_k is the step size in the selected direction. It is straightforward to show that the gradient of this objective function is given by [21], [22]

$$\nabla f(x) = -R_s \int\limits_{\theta\in\Theta} n(q)\varphi(q)d\theta \tag{49}$$

where Θ is the part of the perimeter of the sensing disk that lies inside the outer-bounding polygon, and $n(q)$ is the normal vector to the perimeter pointing outward from the polygon. The search direction p_k is a scaled gradient vector and is updated at each iteration [22]. The value of α_k, on the other hand, is determined by using a line search procedure.

Notice that it is not required to compute the spatial probability function for the whole Voronoi margin in the robust Max-Area approach. The spatial probability function characterizes the importance of the points within the Voronoi margin in terms of coverage objective. However, for implementing the proposed algorithm, this function is required to be computed only for the points on the perimeter of the sensing disk, which lie inside the outer-bounding polygon of a sensor. In fact, to obtain the gradient of the objective function [as characterized by relation (49)], it is only required to perform a numerical integration over an arc. To this end, a set of points are considered on the perimeter of the sensing disk, and subsequently, the term $n(q)\varphi(q)$ is computed for every point q and is added to a summation if the point is inside the outer-bounding polygon.

Once the iterative algorithm given above converges to the optimum point, the final value of the resultant sequence $\{x_k\}$, denoted by x_s^*, is considered as the candidate point for the next position of the sensor. A similar optimization procedure is performed by all sensors in the case of multi-sensor coverage optimization, and each sensor finds the optimum point inside its outer-bounding polygon. Then, the sensor performs a test to check if the coverage increases more than a prescribed percentage by moving to this point. Such a test is considered to achieve network-wide convergence properties. To proceed further, let the following notation be introduced first.

- $\Psi_i^{\text{in}}(k^-)$ is the covered region inside $\Pi_i^{\text{in}}(k^-)$ at the beginning of the kth round.
- $\Psi_i^{\text{in}}(k^+)$ is the region inside $\Pi_i^{\text{in}}(k^-)$ covered by sensor S_i if it moves to the candidate point obtained in the kth round of the algorithm.
- $\Psi_i^{\text{out}}(k^-)$ is the covered region inside $\Pi_i^{\text{out}}(k^-)$ at the beginning of the kth round.
- $\Psi_i^{\text{out-zero}}(k^-)$ is the region inside $\Pi_i^{\text{out}}(k^-)$ with the property $\varphi_i(q) = 0$, which is covered by sensor S_i at the beginning of the kth round.
- $\Psi_i^{\text{out}}(k^+)$ is the region inside $\Pi_i^{\text{out}}(k^-)$ covered by sensor S_i if it moves to the candidate point obtained in the kth round.

- $\Psi_i^{\text{out-one}}(k^+)$ is the region inside $\Pi_i^{\text{out}}(k^-) - \Pi_i^{\text{in}}(k^-)$ with the property $\varphi_i(q) = 1$, which is covered by sensor S_i if it moves to the candidate point obtained in the kth round (note that the region $\Psi_i^{\text{out-one}}(k^+)$ includes all points that are outside the inner-bounding polygon but certainly belong to the true Voronoi polygon).

In the kth round of the algorithm, sensor S_i will move to the candidate point if

$$\left|\Psi_i^{\text{in}}(k^+)\right| + \left|\Psi_i^{\text{out-one}}(k^+)\right| \geq (1+\varepsilon)\left[\left|\Psi_i^{\text{out}}(k^-)\right| - \left|\Psi_i^{\text{out-zero}}(k^-)\right|\right] \quad (50)$$

where $|.|$ denotes the area of the corresponding region (which is a positive real number) and ε is a small positive constant (which is a design parameter). The idea behind (50) is to guarantee that if a sensing agent moves to its candidate point, its local coverage w.r.t. its current *unknown* Voronoi polygon will increase. To this end, the bounding polygons and the spatial probability function are used in the movement condition (50), which states that the sensor will move only if the area that it will certainly cover from the new location is greater than an upper bound for the current covered area by a certain percentage. It will be shown in Section V-B that the above condition ensures the convergent movement of sensors at the network level.

Once the sensors move to the candidate points [in accordance with the movement condition (50)], the new inner- and outer-bounding polygons are constructed, and the algorithm uses the new polygons and new local spatial probability functions subsequently. Eventually, when the local weighted coverage of no sensor increases w.r.t. its outer-bounding polygon (by the percentage described earlier), the algorithm stops.

Example 2: To illustrate the robust Max-Area coverage scheme, a simple case is presented here in which four sensors with similar sensing range of $R_s = 3$ m are deployed in a 10 m × 10 m field. The error in measuring the position of every neighboring sensor is assumed to be less than or equal to 10% of the exact distance. The initial positions of the sensors are randomly selected within the field, resulting in an initial coverage factor of 55%. With the erroneous measurements, the sensors under the proposed algorithm reach the steady-state configuration in four iterations with a final coverage factor of 94%. The evolution of the bounding polygons is demonstrated in Fig. 10, where the inner-bounding and outer-bounding polygons are depicted in dashed and solid lines, respectively. ■

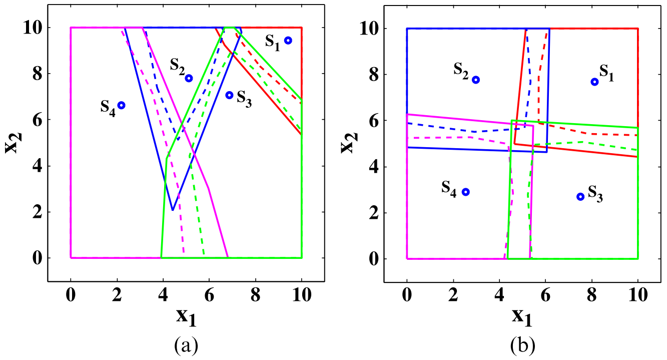

Fig. 10. Evolution of the bounding polygons constructed by the sensors: (a) initial configuration and (b) final configuration.

B. Convergence Properties

The robust Max-Area algorithm presented in the previous subsection uses the local inaccurate information available to each sensor in order to relocate it. It is shown in the present subsection that the movement of every sensor under this strategy is convergent. Starting from the initial configuration, the locations of the sensors after the first round of the algorithm depend on the corresponding position measurements, and can be characterized by a set-valued map. In what follows, some concepts and notations (in particular, Theorem 3) are borrowed from [27], and the convergence properties are proved using LaSalle's invariance principle for set-valued maps. It is desired to show that a Lyapunov function exists for the robust Max-Area coverage strategy, with the required convergence conditions. For this purpose, some preliminary results on the Voronoi-based coverage optimization algorithms are reviewed briefly. Note that these results are related to the traditional Voronoi partitioning of the field with exact position information.

Consider a general Voronoi-based sensor deployment strategy and the scheme reviewed in Section II-A. The following notation will be used to characterize different sets of points in the field.

- $\Pi_i(k^-)$ is the Voronoi polygon containing sensor S_i at the beginning of the kth round of the algorithm.
- $\Psi(k^-)$ is the region in the field which is covered by the sensors at the beginning of the kth round of the algorithm.
- $\Psi_i(k^-)$ is the covered region inside $\Pi_i(k^-)$ at the beginning of the kth round (it is easy to verify that $\Psi_i(k^-)$ is equal to the intersection of $\Pi_i(k^-)$ and the coverage circle of sensor S_i).
- $\Psi_i(k^+)$ is the region inside $\Pi_i(k^-)$ covered by sensor S_i if it moves to the candidate point obtained in the kth round. It is important to note that $\Pi_i(k^-)$ is different from the Voronoi polygon of sensor S_i when it is located at the candidate point obtained in the kth round.

The convergence of a general Voronoi-based coverage strategy in a mobile sensor network is addressed in the following theorem [27, Theorem 2].

Theorem 3: Assume that a set of n mobile sensors are driven by a general distributed Voronoi-based protocol (as described in Section II-A) in a target field that is partitioned by the Voronoi polygons at the beginning of each coverage round. Then, the trajectories of the sensors converge to a set of points (possibly infinitely many) for which the overall weighted coverage is the same, regardless of how the sensors' positions are chosen among the points. Moreover, before reaching the steady state, the overall weighted coverage under the general Voronoi-based strategy increases in each round.

Proof: See [27] for a detailed proof.

It can be shown that under the Max-Area technique, where each sensor moves to the optimal point within its Voronoi polygon (such that the area covered within the polygon is maximized), the total covered area is maximized locally in the final configuration [27]. The following theorem presents the convergence result for a mobile sensor network subject to the position measurement errors.

Theorem 4: Consider a group of mobile sensors with erroneous position measurements, driven by the robust Max-Area deployment strategy. The trajectories of the sensors converge to a set of points with identical coverage factors. Moreover, the total covered area is monotonically increasing, while reaching the steady state.

Proof: Let the evolution of the positions of the sensors in different rounds of the algorithm be described by a set-valued map T_U (the subscript U stands for uncertainty). This means that given a set of deterministic points $X_s(k)$, the positions of the sensors in the next round (i.e. $X_s(k+1)$) belong to the set $T_U[X_s(k)]$. For any sensor configuration, the true Voronoi diagram (corresponding to the real position of the sensors) partitions the field. Considering the notations introduced earlier in this subsection for the true Voronoi diagram, it is desired to prove that $V(X_s(k)) = nA_D - |\Psi(k^-)|$ is a Lyapunov function for the set-valued map $T_U[X_s(k)]$, where $A_D = \pi R_s^2$ is the area of each sensing disk. To this end, it is shown first that $V(X_s(k+1)) \leq V(X_s(k))$ for any $X_s(k+1) \in T_U[X_s(k)]$. Note that at the kth round, sensor S_i uses the set of measured positions of its neighboring sensors to construct its inner-bounding and outer-bounding polygons. These polygons can be different for a different set of measured positions, but the true Voronoi polygon $\Pi_i(k^-)$ is always bounded by the two polygons as shown in Theorem 2. Hence

$$\left|\Psi_i^{\text{in}}(k^-)\right| \leq \left|\Psi_i(k^-)\right| \leq \left|\Psi_i^{\text{out}}(k^-)\right| \tag{51}$$

$$\left|\Psi_i^{\text{in}}(k^+)\right| \leq \left|\Psi_i(k^+)\right| \leq \left|\Psi_i^{\text{out}}(k^+)\right|. \tag{52}$$

A less conservative upper bound for $|\Psi_i(k^-)|$ can be obtained by excluding the points whose probability of being inside the true Voronoi region is zero as characterized by $\varphi_i(.) = 0$, i.e.,

$$\left|\Psi_i^{\text{in}}(k^-)\right| \leq \left|\Psi_i(k^-)\right| \leq \left|\Psi_i^{\text{out}}(k^-)\right| - \left|\Psi_i^{\text{out-zero}}(k^-)\right|. \tag{53}$$

Similarly, a less conservative lower bound for $|\Psi_i(k^+)|$ is obtained by including the points outside $\Pi_i^{\text{in}}(k^-)$ whose probability of being inside the corresponding true Voronoi region is one as characterized by $\varphi_i(.) = 1$. Note that the set containing such points was defined before as $\Psi_i^{\text{out-one}}(k^+)$. Hence

$$\left|\Psi_i^{\text{in}}(k^+)\right| + \left|\Psi_i^{\text{out-one}}(k^+)\right| \leq \left|\Psi_i(k^+)\right| \leq \left|\Psi_i^{\text{out}}(k^+)\right|. \tag{54}$$

Now, for any $X_s(k+1) \in T_U[X_s(k)]$, the relation (50) with $\varepsilon > 0$ implies that $|\Psi_i(k^+)| > |\Psi_i(k^-)|$, and, hence, the local coverage of S_i w.r.t. $\Pi_i(k^-)$ increases in the kth round. The descent property of the candidate Lyapunov function is then concluded from Theorem 3. According to LaSalle's invariance principle for set-valued maps, the sequence $\{X_s(k)\}$ converges to the largest invariant set in $M_U = \{X_s | \exists Y_s \in T_U(X_s); V(Y_s) = V(X_s)\}$ [21]. The convergence of the sensor movement is now deduced from Theorem 3 on noting that X_s converges to a set with the same total coverage. ■

Remark 6: Note that although the true Voronoi polygons are not available, by utilizing the local spatial probability functions $\varphi_i(q)$ and finding the bounding polygons, a convergent movement strategy is the result, as shown in Theorem 4. The theorem also shows that under the robust Max-Area strategy, the total covered area is a monotonic nondecreasing function of time.

C. Comparative Performance Evaluation

In this subsection, the performance of the robust Max-Area algorithm in terms of total coverage and the convergence rate is evaluated and compared with that of Minimax and Max-Area strategies. These two algorithms do not use the knowledge of uncertainty and also do not use the notion of bounding polygons introduced in the present paper. They simply assume that the measurements are accurate and based on that every sensor constructs its Voronoi region. Subsequently, the sensor moves to a new position inside the polygon in order to improve the coverage factor. Since these algorithms do not require local spatial probability functions, they have lower computational complexity. However, ignoring the effect of inaccurate measurements in the Minimax and Max-Area strategies leads to the fluctuating behavior and slow convergence of sensor movements.

To investigate the effect of using bounding polygons instead of the true Voronoi cells (which are not known), two variants of the Minimax strategy, namely the *Inner-Minimax* and *Outer-Minimax* algorithms, are introduced here. Under these algorithms, every sensor constructs its inner-bounding or outer-bounding polygon, and then, similar to the Minimax approach, considers the center of the smallest enclosing disk of the polygon as the candidate point to move to. It is to be noted that these algorithms do not take the local spatial probability functions into consideration and only utilize partial information about the measurement error for constructing the bounding polygons.

Example 3: Consider a network of 30 mobile sensors randomly placed in a 50 m × 50 m field, and let the sensing radius of every sensor be 6 m. The coverage performance under different strategies is evaluated for the case when the position measurements are subject to zero, 5%, 10%, 15%, and 20% error. For each case, 50 different random initial sensor configurations are considered, and five different deployment strategies (including the robust Max-Area strategy) are subsequently used to increase coverage. The performance of each strategy is evaluated by taking the average over all simulations.

Fig. 11(a) depicts the convergence results, which show that the number of rounds it takes for the robust Max-Area algorithm to converge to the desirable neighborhood of the final coverage is less than that for the Minimax and Max-Area algorithms. This demonstrates the energy efficiency of the algorithm introduced in this work because the energy consumption increases with the number of sensor movements (note that after each round of the algorithm every sensor moves, and each move requires the sensor to overcome the static friction). As for the coverage factor, Fig. 11(b) shows that for the case of no measurement error the robust Max-Area algorithm performs the same as the Max-Area algorithm, as expected, and better than the Minimax technique. Note that the better coverage

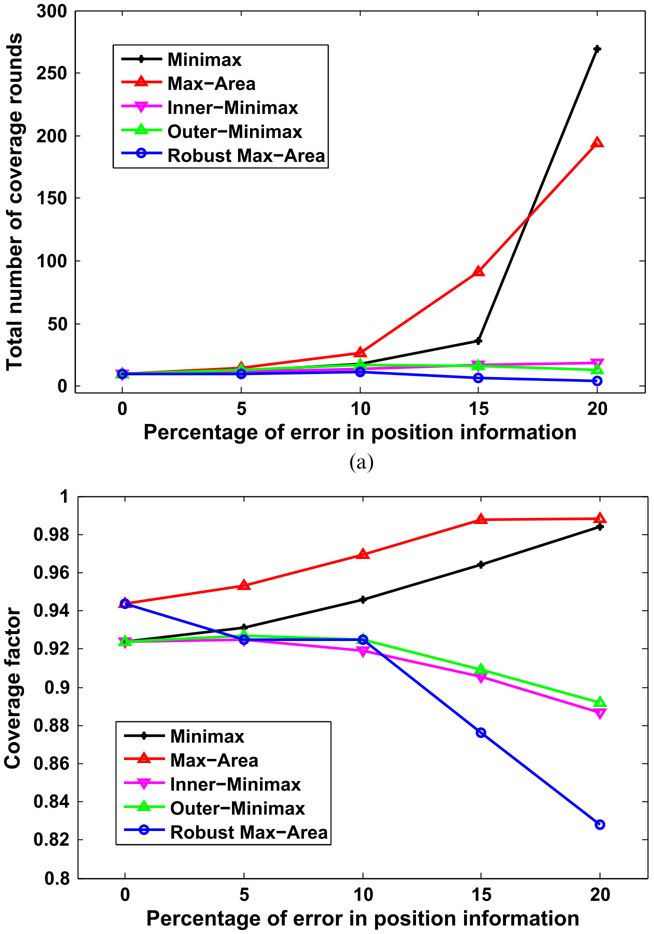

(a)

(b)

Fig. 11. Average performance indicators over 50 simulations for five different coverage optimization strategies with different measurement errors in Example 3. (a) Number of coverage rounds and (b) final coverage factor.

performance comes at the cost of lower convergence rate and higher energy consumption, as discussed above. This introduces a tradeoff between coverage performance and the energy efficiency of the algorithm. In other words, the reliability and guaranteed convergence of the robust Max-Area method in the presence of measurement error compromises coverage performance, to some extent.

It is to be noted that the inner-Minimax and outer-Minimax methods also prove efficient in both increasing the coverage factor and reducing the computation time (which is measured based on the number of coverage rounds). In addition, these *ad hoc* algorithms are computationally simpler than the robust Max-Area approach. However, among all five algorithms, the robust Max-Area scheme is the only one that is analytically proved to converge to a steady-state configuration in the presence of measurement error. ■

VI. Conclusion

The problem of coverage maximization in a mobile sensor network (MSN) subject to measurement errors is studied in this paper. Given the maximum size of the position measurement error, a geometric approach is provided to find two convex polygons, namely inner- and outer-bounding polygons, which the exact Voronoi polygon is guaranteed to lie between them. A probabilistic characterization for the region between the two polygons is given, which is subsequently used to develop a sensor deployment strategy for maximizing network coverage. The robust Max-Area strategy is based on a nonlinear optimization approach which optimally positions the sensing disk inside the outer-bounding polygon. It is shown that under the proposed deployment strategy the movement of the sensors is guaranteed to converge and also the total covered area by the sensors either increases or does not change in consecutive coverage rounds of the algorithm. Simulations demonstrate the effectiveness of the robust Max-Area coverage optimization technique in the presence of position measurement error. Two other algorithms, namely the inner-Minimax and outer-Minimax, are also presented, which partially utilize existing information on the measurement error to position sensors in the field such that coverage increases. The convergence analysis of these two methods is the subject of future research.

Appendix A
Geometric Algorithms to Find Inner-Bounding and Outer-Bounding Polygons

To obtain the inner-bounding polygon of a sensor (formally defined by (40)), one needs to obtain the inner-bounding rays associated with every neighboring sensor and then find the corresponding vertices (the intersection of facets). These facets are described as

$$q_2 - m_{\perp 1} q_1 = \left(q_{ji}^{\text{in}}\right)_2 - m_{\perp 1}\left(q_{ji}^{\text{in}}\right)_1 \tag{55}$$

$$q_2 - m_{\perp 2} q_1 = \left(q_{ji}^{\text{in}}\right)_2 - m_{\perp 2}\left(q_{ji}^{\text{in}}\right)_1. \tag{56}$$

The following algorithm constructs the inner-bounding polygon for sensor S_i. The polygon will be represented by the inequality $H_i^{\text{inner}} q \leq K_i^{\text{inner}}$.

Algorithm I: Obtaining the Inner-Bounding Polygon for S_i

```
I) Initialize the matrices describing the polygon $\Pi_i^{\text{inner}}$ as $H_i^{\text{inner}} = []$ and $K_i^{\text{inner}} = []$.
II) Sort the neighboring sensors based on the measured angle by sensor $S_i$ as defined in (11). Let the indices of the neighboring nodes be contained in the ordered set $N_i$.
III) For $j = 1 : \dim(N_i)$,
    1) Compute $q_{ji}^{\text{in}}$, $\theta_1$, $\theta_2$, $m_{\perp 1}$ and $m_{\perp 2}$ from (4), (10), (11), (12) and (13), respectively.
    2) if $(x_i)_2 - m_{\perp 1}(x_i)_1 \leq (q_{ji}^{\text{in}})_2 - m_{\perp 1}(q_{ji}^{\text{in}})_1$,
       $H_i^{\text{inner}} \leftarrow [H_i^{\text{inner}}; [-m_{\perp 1}, 1]]$ and $K_i^{\text{inner}} \leftarrow [K_i^{\text{inner}}; (q_{ji}^{\text{in}})_2 - m_{\perp 1}(q_{ji}^{\text{in}})_1]$;
       else,
       $H_i^{\text{inner}} \leftarrow [H_i^{\text{inner}}; [m_{\perp 1}, -1]]$ and $K_i^{\text{inner}} \leftarrow [K_i^{\text{inner}}; -(q_{ji}^{\text{in}})_2 + m_{\perp 1}(q_{ji}^{\text{in}})_1]$;
    3) if $(x_i)_2 - m_{\perp 2}(x_i)_1 \leq (q_{ji}^{\text{in}})_2 - m_{\perp 2}(q_{ji}^{\text{in}})_1$,
       $H_i^{\text{inner}} \leftarrow [H_i^{\text{inner}}; [-m_{\perp 2}, 1]]$ and $K_i^{\text{inner}} \leftarrow [K_i^{\text{inner}}; (q_{ji}^{\text{in}})_2 - m_{\perp 2}(q_{ji}^{\text{in}})_1]$;
```

```
  else,
  $H_i^{\text{inner}} \leftarrow [H_i^{\text{inner}}; [m_{\perp 2}, -1]]$ and $K_i^{\text{inner}} \leftarrow [K_i^{\text{inner}}; -(q_{ji}^{\text{in}})_2 + m_{\perp 2}(q_{ji}^{\text{in}})_1]$;
IV) In order to find a minimal representation of the inner-bounding polygon, remove those rows in $H_i^{\text{inner}}$ and $K_i^{\text{inner}}$ which correspond to the redundant facets. ■
```

Note that the conditional statements in step III of the algorithm are to obtain the correct sign for the gains H_i^{inner} and K_i^{inner} describing the facets. Since x_i belongs to Π_i^{inner}, this is done by using (55) and (56), and verifying in which side of each facet the point x_i lies.

Note that if a neighboring sensor is too far from S_i, its inner-bounding rays will not form any of the facets of the inner-bounding polygon of S_i. Such neighboring sensors (and the corresponding outer-bounding rays) are termed *ineffective* here. The approach to find the outer-bounding polygon of a sensor is to disregard its ineffective neighboring sensors and intersect the effective outer-bounding rays of its neighboring sensors in an ordered manner and then to obtain the vertices of the polygon. The intersection points of the outer-bounding rays associated with the effective neighboring sensors are then used to form an ordered set, which is, in fact, the set of points characterizing the outer-bounding polygon of the sensor. The steps of the procedure described above are summarized in the following algorithm (note that the inner-bounding polygon of S_i is assumed to be obtained beforehand).

Algorithm II: Obtaining the Outer-Bounding Polygon for S_i

```
I) Initialize the set of vertices describing the polygon $\Pi_i^{\text{outer}}$ as $V_i^{\text{outer}} = \{\}$.
II) Initialize the set of indices of the effective sensors as $N_i^{\text{eff}} = \{\}$, and then use the following procedure to find such sensors one-by-one:
  For $j = 1 : \dim(N_i)$,
    1) Compute $q_{ji}^{\text{in}}, \theta_1, \theta_2, m_{\perp 1}$ and $m_{\perp 2}$ from (4), (10), (11), (12) and (13), respectively.
    2) If any of the two lines (55) and (56) form a facet of $\Pi_i^{\text{inner}}$, then $N_i^{\text{eff}} = N_i^{\text{eff}} \cup \{j\}$.
III) Sort the indices of the effective neighboring sensors in $N_i^{\text{eff}}$ based on the angle viewed by sensor $S_i$ as provided in (11). Let the new ordered set of indices be denoted by $\bar{N}_i^{\text{eff}}$.
IV) For $k = 1 : \dim(\bar{N}_i^{\text{eff}})$,
    1) Obtain two pairs of outer-bounding rays associated with sensors $k$ and $k+1$ using (18) and (19). If $k = \dim(\bar{N}_i^{\text{eff}})$, then obtain the rays for sensors $k$ and 1.
    2) Obtain every intersection point of the two pairs of outer-bounding rays obtained in step (IV-1), and denote it by $p_k$. Set $V_i^{\text{outer}} = V_i^{\text{outer}} \cup \{p_k\}$.
V) The outer-bounding polygon is characterized by the convex hull of the points in $V_i^{\text{outer}}$. ■
```

Note that the details of some geometric procedures in the above algorithm (e.g., finding the intersection points of two pairs of rays in step IV-2) are omitted for brevity. Note also that both algorithms only use information available to sensor S_i, and, hence, they operate in a distributed fashion.

REFERENCES

[1] A. Mainwaring, D. Culler, J. Polastre, R. Szewczyk, and J. Anderson, "Wireless sensor networks for habitat monitoring," in *Proc. 1st ACM Int. Workshop Wireless Sensor Netw. Appl.*, 2002, pp. 88–97.

[2] D. Estrin, R. Govindan, J. Heidemann, and S. Kumar, "Next century challenges: Scalable coordination in sensor networks," in *Proc. 5th Annu. ACM/IEEE Int. Conf. Mobile Comput. Netw.*, 1999, pp. 263–270.

[3] T. He, S. Krishnamurthy, J. Stankovic, T. Abdelzaher, L. Luo, R. Stoleru, T. Yan, L. Gu, J. Hui, and B. Krogh, "Energy-efficient surveillance system using wireless sensor networks," in *Proc. 2nd Int. Conf. Mobile Syst., Appl., Services*, 2004, pp. 270–283.

[4] S. Poduri and G. Sukhatme, "Constrained coverage for mobile sensor networks," in *Proc. IEEE Int. Conf. Robot. Autom.*, 2004, vol. 1, pp. 165–171.

[5] Y. Zou and K. Chakrabarty, "Distributed mobility management for target tracking in mobile sensor networks," *IEEE Trans. Mobile Comput.*, vol. 6, no. 8, pp. 872–887, 2007.

[6] J. Cortés, S. Martínez, T. Karatas, and F. Bullo, "Coverage control for mobile sensing networks," *IEEE Trans. Robot. Autom.*, vol. 20, no. 2, pp. 243–255, 2004.

[7] G. Wang, G. Cao, and T. La Porta, "Movement-assisted sensor deployment," *IEEE Trans. Mobile Comput.*, vol. 5, no. 6, pp. 640–652, 2006.

[8] G. Nicholls, D. Kourie, and T. Strauss, "Sensitivity analysis of Voronoi-based sensor deployment and reconfiguration algorithms," *South African Comput. J.*, pp. 35–43, 2009.

[9] Y. Mostofi and R. Murray, "Communication and sensing trade-offs in cooperative mobile networks," *Asian J. Control*, vol. 10, no. 2, pp. 156–170, 2008.

[10] Y. Wang and I. Hussein, "Awareness coverage control over large-scale domains with intermittent communications," *IEEE Trans. Autom. Control*, vol. 55, no. 8, pp. 1850–1859, 2010.

[11] C. Nowzari and J. Cortés, "Self-triggered coordination of robotic networks for optimal deployment," *Automatica*, vol. 48, no. 6, pp. 1077–1087, 2012.

[12] R. Carli and F. Bullo, "Quantized coordination algorithms for rendezvous and deployment," *SIAM J. Control Optim.*, vol. 48, no. 3, pp. 1251–1274, 2009.

[13] Q. Wu, N. Rao, X. Du, S. Iyengar, and V. Vaishnavi, "On efficient deployment of sensors on planar grid," *Comput. Commun.*, vol. 30, no. 14–15, pp. 2721–2734, 2007.

[14] H. Ammari, "Stochastic k-coverage in wireless sensor networks," *Wireless Algorithms, Syst., Appl.*, pp. 125–134, 2009.

[15] A. Hossain, P. Biswas, and S. Chakrabarti, "Sensing models and its impact on network coverage in wireless sensor network," in *Proc. IEEE Region 10 3rd Int. Conf. Ind. Inf. Syst.*, 2008, pp. 1–5.

[16] M. Hefeeda and H. Ahmadi, "Energy-efficient protocol for deterministic and probabilistic coverage in sensor networks," *IEEE Trans. Parallel Distrib. Syst.*, vol. 21, no. 5, pp. 579–593, 2010.

[17] Y. Zou and K. Chakrabarty, "Uncertainty-aware and coverage-oriented deployment for sensor networks," *J. Parallel Distrib. Comput.*, vol. 64, no. 7, pp. 788–798, 2004.

[18] S. Mal-Sarkar, I. Sikder, C. Yu, and V. Konangi, "Uncertainty-aware wireless sensor networks," *Int. J. Mobile Commun.*, vol. 7, no. 3, pp. 330–345, 2009.

[19] J. Durham, R. Carli, P. Frasca, and F. Bullo, "Discrete partitioning and coverage control for gossiping robots," *IEEE Trans. Robot.*, vol. 28, no. 2, pp. 364–378, 2012.

[20] J. Habibi, H. Mahboubi, and A. Aghdam, "Distributed coverage optimization in a network of mobile agents subject to measurement error," in *Proc. Amer. Control Conf.*, 2012, pp. 4510–4515.

[21] J. Cortés, S. Martínez, and F. Bullo, "Spatially-distributed coverage optimization and control with limited-range interactions," *ESAIM: Control, Optim. Calculus of Variations*, vol. 11, no. 4, pp. 691–719, 2005.

[22] J. Habibi, H. Mahboubi, and A. G. Aghdam, "A nonlinear optimization approach to coverage problem in mobile sensor networks," in *Proc. 50th IEEE Conf. Decision Control/Eur. Control Conf.*, 2011, pp. 7255–7261.

[23] H. Mahboubi, K. Moezzi, A. G. Aghdam, K. Sayrafian-Pour, and V. Marbukh, "Distributed deployment algorithms for improved coverage in mobile sensor networks," in *Proc. IEEE Multiconf. Syst. Control*, 2011, pp. 1244–1249.

[24] J. Sember and W. Evans, "Guaranteed Voronoi diagrams of uncertain sites," in *Proc. 20th Annu. Can. Conf. Comput. Geometry*, 2008, pp. 207–210.

[25] R. Cheng, X. Xie, M. Yiu, J. Chen, and L. Sun, "UV-diagram: A Voronoi diagram for uncertain data," in *Proc. 26th IEEE Int. Conf. Data Eng.*, 2010, pp. 796–807.

[26] E. W. Weisstein, "Circle-Circle Intersection, From Mathworld—A Wolfram Web Resource." [Online]. Available: http://mathworld.wolfram.com/Circle-CircleIntersection.html, accessed December 2012.

[27] J. Habibi, H. Mahboubi, and A. G. Aghdam, "A gradient-based coverage optimization strategy for mobile sensor networks," *IEEE Trans. Control Netw. Syst.*, 2015, doi: 10.1109/TCNS.2016.2515370, preprint.

Jalal Habibi (S'07–M'09–SM'13) received the B.Sc. and M.A.Sc. degrees in electrical engineering from Sharif University of Technology, Tehran, Iran, in 1997 and 2000, respectively, and the Ph.D. degree from the University of Tehran, Tehran, Iran, in 2008.

He was a visiting Ph.D. student at the Automatic Control Laboratory of ETH Zurich, Switzerland, from February 2006 to July 2007. He was an Assistant Professor at the Science and Research Branch of Azad University, Tehran, Iran, from 2009 to 2010. He was a Research Associate at the Department of Electrical and Computer Engineering, Concordia University, Montreal, QC, Canada, from 2010 to 2015, and is currently a Research Associate at the Faculty of Engineering of McGill University, Montreal, QC, Canada. His research interests include predictive control, hybrid systems, mathematical optimization, sensor networks, and wireless communications.

Dr. Habibi is an Associate Editor of the *Canadian Journal of Electrical and Computer Engineering* and a member of Professional Engineers Ontario. He has been a member of the Technical Program Committee of a number of conferences, including the IEEE International Conference on Wireless for Space and Extreme Environments (IEEE WiSEE) and the International Conference on Advances in Computing, Communications and Informatics.

Hamid Mahboubi (S'08–M'14–SM'15) received the B.Sc. degree in electrical engineering in 2003 from Sharif University of Technology, Tehran, Iran, where he was awarded an honorary admission, the M.A.Sc. degree in electrical and computer engineering from the University of Tehran, Tehran, Iran, in 2006, and the Ph.D. degree from Concordia University, Montreal, QC, Canada, in 2014.

He is currently a postdoctoral fellow in the Department of Electrical and Computer Engineering at McGill University, Montreal, QC, Canada. His research interests include mobile sensor networks, multi-agent systems, hybrid systems, networked control systems, smart grids, and optimization.

Dr. Mahboubi is the recipient of Natural Sciences and Engineering Research Council of Canada (NSERC) Postdoctoral Fellowship, Concordia University Distinguished Doctoral Dissertation Prize in Engineering and Natural Sciences, Doctoral Prize in Engineering and Computer Science, Fonds québécois de la recherche sur la nature et les technologies (FQRNT) Post-Doctoral Award, Bourse d'Etudes Hydro Quebec Scholarship, Power Corporation of Canada Graduate Fellowship, and Canadian National Award in Transportation. He is a recipient of the Governor General of Canada Academic Gold Medal in 2015, and he is also a recipient of the Gold Medal in the 1999 National Math Olympiad in Iran. He has served as Chair of the Control Systems Chapter of the IEEE Montreal Section since January 2012. He is a member of the Editorial Board of *IEEE SigView* (IEEE Signal Processing Society). He was also a member of the Technical Program Committee of 2015 IEEE International Conference on Wireless for Space and Extreme Environments.

Amir G. Aghdam (S'96–M'00–SM'05) received the Ph.D. degree in electrical and computer engineering from the University of Toronto, Toronto, ON, Canada, in 2000.

He is currently a Professor in the Department of Electrical and Computer Engineering at Concordia University, Montreal, QC, Canada, and an Associate Dean of The School of Graduate Studies (Student Affairs and Postdoctoral Studies). He is a member of Professional Engineers Ontario. His research interests include multi-agent networks, distributed control, optimization and sampled-data systems.

Dr. Aghdam is a member of the Conference Editorial Board of IEEE Control Systems Society, Co-Editor-in-Chief of the IEEE SYSTEMS JOURNAL, an Associate Editor of the IEEE TRANSACTIONS ON CONTROL SYSTEMS TECHNOLOGY, the *European Journal of Control*, the *IET Control Theory & Applications*, and the *Canadian Journal of Electrical and Computer Engineering*. He has been a member of the Technical Program Committee of a number of conferences, including the IEEE Conference on Systems, Man and Cybernetics (IEEE SMC), the IEEE Conference on Decision and Control (IEEE CDC), and the IEEE Multiconference on Systems and Control (IEEE MSC). He was a member of the Review Committee for the Italian Research and University Evaluation Agency (ANVUR) for 2012–2013, and a member of the Natural Sciences and Engineering Research Council of Canada (NSERC) ECE Evaluation Group for 2014–2016. He is a recipient of the 2009 IEEE MGA Achievement Award and the 2011 IEEE Canada J. J. Archambault Eastern Canada Merit Award. He was the 2014–2015 President of IEEE Canada and Director (Region 7), IEEE, Inc., and was also a member of the IEEE Awards Board for this period. He was a Visiting Scholar at Harvard University in fall 2015, and is currently an Associate at the Harvard Paulson School of Engineering. His research interests include multi-agent networks, distributed control, optimization and sampled-data systems.